Radar Sensor Signal Acquisition and Multidimensional FFT Processing for Surveillance Applications in Transport Systems

Sergio Saponara, *Senior Member, IEEE*, and Bruno Neri

***Abstract*— The design and test of a radio detection and ranging (Radar) sensor signal acquisition and processing platform is presented in this paper. The Radar sensor operates in real time and is suited for surveillance applications in transport systems. It includes a front-end with a continuous-wave frequency-modulated transceiver operating in X-band, with a single transmitter and multiple receivers, and a multichannel high-speed A/D converter. Sensor signal processing and data communication tasks with external hosts are managed by a field-programmable gate array. The signal processing chain includes region of interest selection, multidimensional fast Fourier transform, peak detection, alarm decision logic, data calibration, and diagnostic. By configuring the Radar sensing platform in low-power mode (7-dBm transmitted power), it is possible to detect still and moving targets with a covered range up to 300-m and 30-cm resolution. The measuring range can be increased up to 2 km by adding an extra 34.5-dBm power amplifier. The Radar sensing platform can be configured for a maximum detected speed of 200 km/h, with a resolution of 1.56 km/h, or a speed up to 50 km/h with a resolution of 0.4 km/h. The cross-range resolution depends on the number of receiving channels; a tradeoff can be found between cross-range resolution of the Radar sensor and its complexity and power consumption. With respect to the state of the art of surveillance Radar sensors and light detection and ranging, the proposed solution stands for its high configurability and for the better tradeoff that can be found in terms of covered distance and power consumption.**

***Index Terms*— 3-D fast Fourier transform (FFT), field-programmable gate array (FPGA), light detection and ranging (Lidar), radio detection and ranging (Radar) sensor, sensor signal processing, surveillance sensors.**

I. Introduction

SMART transportation systems for surveillance, or for driving assistance, require robust sensing platforms, tolerant to bad light and weather conditions [1]–[12]. Radio detection and ranging (Radar) sensors can allow for robust detection of targets and measurement of their speed, distance, and motion direction. Traditionally, Radar sensing platforms have been realized for defence applications or for surveillance of big infrastructures [13]–[18], e.g., airports, or large areas, e.g., remote monitoring of land and coastal borders or bay areas. The proposed sensors typically result in a cost and size too high for civil applications in smart transport systems. Low-cost and low-power Radar sensing solutions have been recently proposed in the literature such as the 60-GHz Radar in [19]–[21] for proximity detection, or low-power ultrawideband (UWB) Radar sensors for measuring vital signs in [22]–[25]. However, in the above cases, the covered range is limited to few meters, and hence the sensors are not suited for land and maritime transport surveillance applications. When monitoring a railroad crossing, a road crossing, or a parking, the needed detection range is in the order of hundreds of meters. Extending the requirement to maritime applications such as monitoring the ingress/egress traffic of a harbor [16], [26], the range distance to be covered is above 1 km.

To address these issues, this paper presents the design and test of a Radar sensor acquisition and processing platform that features high configurability, bounded power consumption, and performance suited for applications in land and maritime transport systems. Hereafter, Section II reviews the state of the art of Radar sensing systems and of other competing technologies to detect still or moving objects and to measure their motion parameters. Radar sensor specifications for some transport applications are discussed in Section III. Section IV details the design of the Radar sensor mixed-signal front-end (transceiver and A/D conversion). Section V deals with the signal processing chain, whereas Section VI discusses its implementation with FPGA technology. The experimental results for example applications in transport systems are discussed in Section VII. Section VIII presents a comparison of the proposed solution with the state of the art and draws some conclusions.

This paper extends [27] in terms of the following:

1) new theoretical results (e.g., the cross-range range resolution analysis and the use of extra power amplifier stage to increase the covered stage);
2) review of state-of-the-art mobility sensors [Radars, light detection and ranging (Lidar), video cameras, and induction loops] in Section II and performance comparison in Section VIII with Radars and Lidars;
3) new design and implementation results (e.g., the tradeoff among number of receiving channels, characteristics of the transmitting channel, performance of the

Manuscript received September 9, 2016; accepted October 21, 2016. Date of publication January 2, 2017; date of current version March 8, 2017. The Associate Editor coordinating the review process was Dr. Salvatore Baglio.

The authors are with the Department of Information Engineering, University of Pisa, 56122 Pisa, Italy (e-mail: sergio.saponara@iet.unipi.it).

Color versions of one or more of the figures in this paper are available online at http://ieeexplore.ieee.org.

Digital Object Identifier 10.1109/TIM.2016.2640518

Radar sensor, and its cost in terms of power consumption and circuit complexity);
4) new experimental results in Section VII (e.g., measurements at a distance above 1 km).

The main contribution of this paper versus the state of the art is highlighted as follows.

1) The configurability of the maximum transmitted power, which allows for different tradeoffs between the Radar power consumption and the maximum covered range, which can be 300 m in low-power mode or 2 km in full-range mode.
2) The configurability of the number of receiving channels (up to eight), which allows for different tradeoffs between angular resolution and the power consumption.
3) Real-time implementation of signal processing tasks on the Artix-7 low-cost and low-power FPGA family, thus saving power versus state-of-the-art designs using graphical processing units (GPUs) and general purpose processors (GPPs).
4) Radar parametric analysis, which highlights the interdependencies existing among Radar performance and analog and digital circuit parameters. This allows a codesign of the mixed-signal transceiver with the FPGA-based digital signal processing, and a tradeoff between the Radar performance and its implementation complexity.
5) Application of the same surveillance Radar to maritime and land applications (in Section VII surveillance for ingress/ egress of ships in a harbor, monitoring of a railroad crossing and of a car parking), whereas the works at the state of the art usually present Radars dedicated to a specific application.

II. Review of State-of-the-Art Mobility Sensors

At the state of the art, the sensing technologies used to detect the presence of a target, and to measure its distance, motion direction, and speed, are Lidars, also known as laser scanners, thermal cameras, RGB and depth cameras, or Radars.

A Lidar is an active sensor, which allows measurements of distance with high resolution and, through time-of-flight processing, also of speed. The SICK LMS 291 used in [28]–[30] is able to scan a scene with a 180° horizontal field of view (FOV) and 0.25° angular resolution (azimuth). Its measuring range is up to 80 m with a resolution of few centimeters. The Lidar active sensors from Velodyne, such as the HDL-64E [1] also adopted for the proof-of-concept Google self-driving car and the HDL-32E [31], have further enhanced performances. The HDL-32E has 360° horizontal FOV, 20° vertical FOV, and it allows for obstacle detection with an angular resolution 0.1° (azimuth) and a distance resolution of 2 cm in the range from 1 up to 100 m. However, Lidars may be cumbersome and costly sensors. The LMS 291 in [28]–[30] has a weight of 4.5 kg and a power consumption of 20 W from a 24 V dc supply. Its cost is about U.S. $ 6000. The HDL-32E has lower weight, 1.3 kg, and lower power consumption, 12 W, but for a cost of about U.S. $ 10 000. The cost of the HDL-64E is about U.S. $ 70 000. The cost, several thousands of euros, and the maximum distance, typically limited to hundreds of meters for those proposed for civil transport applications, are the main bottlenecks of Lidars.

Concerning the maximum distance to be reached, Lidars for long-range sensing have been recently announced in [32] and [33], which target mainly defense applications. The Lidar in [32] and [33] incorporates an array of Geiger mode (GM) single-photon detectors, following the original development of MIT Lincoln lab in [34], and then optimized by Princetonlightwave [35] and Spectrolab [36] companies. The GM Lidar from MIT Lincoln lab [34] has a nominal detection range of 150 m, a range resolution of 40 cm, and an FOV of 10.8° (horizontal). The Lidar weight is about 13.6 kg, and the cost is not reported. The Spectrolab SpectroScan 3-D LIDAR system model MLS 201 has an FOV of 60° (horizontal), a detection range of 20 m, a sample spacing of 0.1 m, an angular resolution of 0.2°, 30 W of power consumption, and a weight of about 2.3 kg. The Kestrel GM 3-D Lidar from Princetonlightwave [35] is used with a resolution of 3.75 cm and a range depth of 300 m. In [32], [33], and [35], increasing the detection range capability can be done but with a tradeoff with other performances that get worse. For example, in [35], there is a proportional tradeoff between distance and resolution, which changes from 3.75 cm at 300-m detection distance to 18.75 cm at 1500-m detection distance. Therefore, further extending the range to 9 km, as declared in [32] and [33], the resolution should further get worse, about 112 cm at 9 km. The Kestrel sensor has a weight of 1.4 kg and a cubic size of 10 cm per side. The power dissipation is 16 W. For the GM 3-D Lidar system in [32] and [33], for defense applications, the weight, cost, power consumption of the whole system, as well as other characteristics such as FOV, distance, or angular resolution are not reported.

Arrays of video cameras and/or ultrasound sensors and/or infrared sensors have been proposed in [11], [12], [28], [30], and [37]–[39] for obstacle detection. They allow for low-cost and low-power recognition and classification of target, thanks to the evolution of CMOS camera-on-chip technology. However, the detection range and the measurements of distance and speed with video cameras are typically limited to tens of meters. As a consequence, target applications are limited to parking assistance of cars or obstacle detection at low speed in crowded urban traffic. Moreover, camera sensors operating in the visible spectrum are not robust in case of bad weather and light conditions. By adding also thermal cameras, operating in long-wave infrared (LWIR, wavelength from 7 to 14 μm) spectrum range, thus creating a multicamera multispectral system, the detection and measurement activities become more robust to bad operating conditions (e.g., sun glares, low light, and fog). However, the maximum covered range is still limited to tens of meters and the increased robustness is paid in terms of increased cost, thousands of euros for multispectral video measuring systems including an LWIR camera with Video Graphics Array (640×480) resolution.

Radar technology, especially operating in the X-band (from 8 to 12 GHz), is preferable to the above competing sensing technologies for smart mobility surveillance. In a range up to few kilometers, covering most of surveillance mobility applications, Radar is less sensitive to weather conditions than

its competitors, allowing for a safe detection of obstacles during heavy rain, snow, and hail, in the presence of dense fog, strong sun glares, and environmental noises and vibration. Radar sensing is also preferable to nonimaging technologies, like induction loops and photoelectric or RF interruption beam sensors, due to its relatively small size compared with the level crossing area and its easier installation, use, and maintenance. However, at the state of the art, most Radar sensors are too cumbersome or power hungry. The pulse compression Radar in [17] operates in Ku-band (12–18 GHz) with a transmitted power of 8 W. It has a detection range from 20 m to 3.7 km with a range resolution of 5 m. The total power consumption is 130 W and the weight is 35 kg. The 32-kW peak power for the pulsed Radar in [18] allows for a 45-km covered range with further increased size and weight versus [17]. The cost of these Radars is in the order of tens of thousands of U.S. dollars. The above characteristics are not suited for applications with limited budgets in terms of cost, power consumption, size, and weight. Compact Radars operating at millimeter waves (e.g., 22–24 GHz in [40]–[43], 77–79 GHz in [44] and [45], 60 GHz in [19]–[21], 80 GHz in [46], 90 GHz in [47], and 300 GHz in [48]) have been recently proposed, such as the long-range radar third generation sensor technology from Bosch [44]. This Radar sensor allows for target detection up to 200–250 m, with a resolution of 10 cm. The FOV is 30°; no rotating elements are used. The typical power consumption is 4 W, and the weight is about 300 g. However, for surveillance applications in small harbor or in large parking, an area of 250 m may be not enough. The covered distance with 60-GHz Radar sensors proposed in [19]–[21] or 80-GHz sensor in [46] is lower, limited to few meters. The attenuation of air and vapor at millimeter waves is at least one order of magnitude higher than in X-band. Thus, reaching distances above 1 km with millimeter-wave Radars would require a too high transmitted power [47]. At lower frequencies, UWB or continuous-wave (CW) Radars have been proposed in [22]–[25] and [49]–[55]. Target applications are vital sign monitoring through contactless measurements of chest or heart displacements or contactless measurements in harsh industrial scenarios. However, in all the above references, the covered distance is limited to few meters.

III. Radar Sensing Platform Specifications

The Radar sensing platform for surveillance application in transport systems has been designed considering the following aspects. The targets to be detected are still or moving obstacles like vehicles (cars, bikes, trucks, ships, and rolling stocks), people, or animals suddenly crossing the road or the rail, with a Radar cross section from few meters to hundreds of square meters. The relevant materials are metal, wood, stone, heavy plastic, and organic materials, which can be easily detected by a Radar sensor [16]. The maximum speed to be detected can be up to 50 km/h in urban scenarios or for trains passing at a railroad crossing or for ships (whose typical speed is around 20 knots, i.e., 37 km/h) or up to few hundreds of km/h in highways or for high-speed trains. The detection range to be covered is from few meters in urban scenario to 300 m in highway scenario, large car parking, or surveillance of smart cities from an unmanned aerial vehicle (UAV). When monitoring a harbor, the covered range can be above 1 km.

TABLE I
X-Band FMCW Radar Sensor Specifications

V_{MAX} (and v_R), km/h	B_W, MHz	d_R, m	D, m	P_{TX}, dBm
50 (0.4) or 200 (1.56)	500	0.3	300	7
50 (0.4) or 200 (1.56)	75	2	2000	34.5

Table I reports the main Radar sensor specifications of this paper in terms of bandwidth of the Radar transceiver (B_W), maximum transmitted power P_{TX}, maximum detection distance along the radial direction D, distance resolution d_R, speed resolution v_R, and maximum detected relative speed (absolute value) between the sensor and the target V_{MAX}.

The X-band is a good choice for Radar working frequency, being a tradeoff among dimensions of sensors and antennas (the wavelength at 10 GHz is 3 cm), working bandwidth, resolution, range of use, capability of standard silicon technologies to operate at such frequency, and environmental conditions. Reference [56] proved that rainfall, snowfall, and fog cause negligible drawbacks on the Radar sensor detection capability because the wavelength at X-band is much bigger than the water droplets and ice crystals of these weather phenomena. To keep low the power consumption and the electromagnetic interference, the best choice is a frequency-modulated (FM) CW Radar. Differently from pulsed Radars, emitting high peak power pulses (hundreds of watts or even kilowatts), the FMCW Radar emits continuously much lower power levels working with the same signal-to-noise ratio (SNR). Using an FMCW scheme, we can exploit integrated power amplifiers instead of cumbersome and costly high-power high-frequency transmission systems like klystron and magnetron typical of pulsed Radars. As it will be shown in Section VII (see Fig. 7), to ensure an SNR higher than 15 dB at receiver side, a target distance D of 300 m can be covered with a transmitter power P_{TX} limited to 7 dBm. To reach a maximum distance D of 2 km, an extra power stage is added providing $P_{\mathrm{TX}} = 34.5$ dBm at the antenna. Range and speed resolutions have been chosen to match typical obstacles dimensions of civil transportation systems. To keep low the sensing system complexity and the power consumption, a coarse resolution is adopted when increasing the maximum measuring range. Therefore, the proposed Radar sensing system has been sized for resolutions d_R of 30 cm and 2 m when the maximum radial distances D are 300 m and 2 km, respectively. To reach these resolutions, the bandwidth (B_W) of the transceiver should be sized from (1), where c is $3 \cdot 10^8$ m/s in free space. The speed resolution v_R is 0.4 and 1.56 km/h when the maximum detected speed V_{MAX} is 50 and 200 km/h, respectively

$$B_W = \frac{c}{2d_R}. \tag{1}$$

IV. Design of Radar Sensor Mixed-Signal Front-End

A. Radar Sensor Front-End Design

Fig. 1 shows the architecture of the FMCW Radar sensor front-end using one transmitter and $M_R = 4$ receivers.

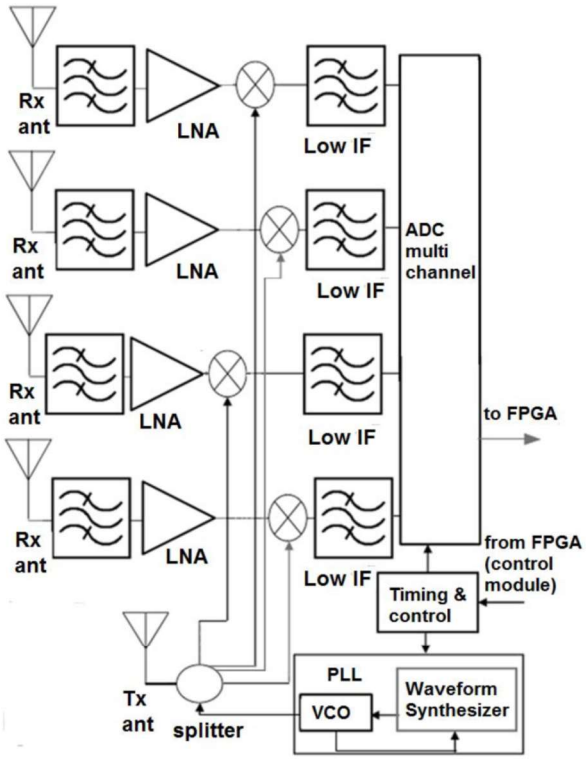

Fig. 1. X-band FMCW Radar sensor mixed-signal front-end, $M_R = 4$.

The architecture is scalable in terms of receiving channels and can be implemented as a microwave board, assembling commercial off-the-shelf chipsets for the main building blocks. To reduce system cost and size, a fixed antenna approach has been followed, and hence there are no moving parts in the Radar sensing system. The FMCW Radar operates at a maximum bandwidth of 500 MHz around 10 GHz (see Table I).

To also detect the direction of arrival of targets, multiple receiving channels have to be used. As reported in [26], for an FMCW, using a patch antenna array with M_R receiving elements each at distance d_{AN}, the angle resolution $\Delta\theta$, and its minimum at boresight is reported in (2). Equation (3) shows the corresponding cross-range resolution $R = D \cdot \Delta\theta$. The size of the patch antenna array is about $M_R \cdot d_{\mathrm{AN}}$. The gain of the patch array receiving antenna varies from about 5.5 dBi with one element up to 12.2 dBi with eight elements

$$\Delta\theta = \frac{\lambda}{2 \cdot (M_R - 1) \cdot d_{\mathrm{AN}} \cdot \cos(\theta)} \Rightarrow \Delta\theta_{\min} = \frac{\lambda}{2 \cdot (M_R - 1) \cdot d_{\mathrm{AN}}} \quad (2)$$

$$R(\theta) = \Delta\theta \cdot D \Rightarrow R_{\min} = \frac{\lambda \cdot D}{2 \cdot (M_R - 1) \cdot d_{\mathrm{AN}}}. \quad (3)$$

For example, with $M_R = 8$, and using a patch antenna array with $d_{\mathrm{AN}} = \lambda$, it is possible to achieve a cross-range resolution of about 1.6 m, which is the typical width of a medium car, at a distance of 23 m, which is the stopping distance at 30 m/h (i.e., 48 km/h). The stopping distance is calculated

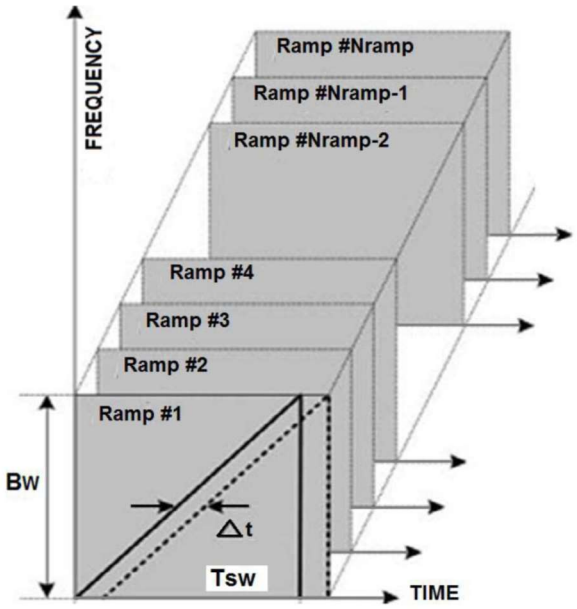

Fig. 2. Linear FMCW ramps transmitted/received by a Radar sensor.

by adding the thinking distance and the braking distance. The corresponding angle resolution is 4.1°. This resolution can be further improved implementing complex algorithms, such as multiple signal classification [57] in the digital signal processing domain, which is out of the scope of this paper. The length of the receiving patch antenna, realized as uniform linear array, is 24 cm with $M_R = 8$.

As far as the transmitter antenna is concerned, a Fabry-Perot resonating topology, as in [58], is used. This antenna features a gain of 13.4 dBi, an S11 return loss below -10 dB in the bandwidth of interest, a size at 10 GHz of 7.2×7.2 cm^2, and a half power beamwidth of $\pm 30°$ in azimuth.

The single-channel transmitting section in Fig. 1, thanks to a phase locked loop (PLL), generates the FMCW signal by modulating the output frequency continuously according to a periodic linear sweep (saw-tooth) in a maximum range of $B_W = 500$ MHz around 10 GHz (see Fig. 2).

The selected waveform synthesizer [59] and the voltage controlled oscillator [60], forming the PLL, allow for the generation of an FMCW output with a linearly varying instantaneous frequency $f(t) = K \cdot t$, where K is the chirp rate and its maximum value is $K = 3.7 \cdot (10^{12}/s^2)$. Given in Fig. 2 a sweep time T_{SW} of 135 μs, the PLL permits to obtain the maximum value of $B_W = 500$ MHz in Table I, which corresponds to a range resolution of 30 cm.

The selected VCO has a maximum output power of 7 dBm, which as proved in Section VII (see Fig. 7) is enough to reach a Radar covered distance of 300 m, thus avoiding cumbersome high-power amplifier stages, as in [17] and [18]. In case an echo is received, due to the presence of a target, the time-of-flight delay along the radial distance D causes a frequency shift of the received FMCW signal versus the FMCW transmitted one. Therefore, the frequency range of the

beat signal that appears at the output of the mixer depends on the maximum distance D to be covered. For a coverage range up to 300 m, the frequency content of the beat signal f_{BEAT} at intermediate frequency (IF), at the output of the mixer, is up to 7.4 MHz. The received signal also has a frequency shift due to Doppler effect, which depends on the relative speed between the target and the Radar sensor. In case of a maximum detected speed V_{MAX} of 200 km/h, i.e., almost 55.5 m/s, the Doppler shift is limited to 3.7 kHz around the above calculated beat signal. A sixth-order low-pass filter, with a bandpass in accordance with the IF content, is used as antialiasing filter before sampling the beat signal with an A/D converter (ADC) at Nyquist rate (15 MS/s per channel).

As far as the receiver path is concerned, the total receiver gain for each of the M_R channels is 72 dB, of which 28 dB is due to the low-noise amplifier (LNA), whereas the remaining 44 dB of gain is obtained in the active mixer stage and in the IF amplifier stage. The noise figure for each receiving channel is 4.2 dB, which according to the Friis formula is de facto determined by the noise figure of the LNA.

B. Radar Sensor Scalability

The analog received signals are converted through a multichannel pipeline ADC. According to (3), depending on the required cross-range resolution, a different number of receiving channels M_R has to be used, and hence a different A/D converting board has to be selected. If only range and speed data are needed, a low-power and single-channel ADC is used such as the ADS9649-20. It provides a sampling rate up to 20 MS/s with a power consumption of 45 mW with a power supply of 1.8 V. It has 14 nominal bits and a signal to noise and distortion ratio of about 72 dB corresponding to 12 effective number of bits (ENOBs). To achieve also angle and hence cross-range information from the Radar sensor, the number of receiving channels has to be increased. The maximum supported number of channels in this paper is eight by the AD9681 device, which allows for a sampling rate of 125 MS/s (i.e., 15.625 MS/s per channel). Its power consumption is 880 mW, i.e., 110 mW/channel with a power supply of 1.8 V. The performance in terms of nominal bit resolution, 14, and ENOB, at least 12, is the same of lower channel solutions. By targeting the same value of nominal bits and ENOB, for four channels, the AD9253-80 provides a sampling rate of 80 MS/s (20 MS/s per channel) and a power consumption of 280 mW, i.e., 70 mW/channel, with a power supply of 1.8 V.

Before the transceiver realization, several simulations have been carried out both at the circuit and system levels using ADS (Agilent Technologies) CAD environment. Realizing the receiver channels, the transmitter channel, and the ADC section in separated boards, it makes easier the proof-of-concept prototype realization and test and the scalability of the final Radar sensor assembly. The snapshot of a single microwave board (that for a receiver channel) has been already reported in [27]. Depending on the number of desired channels (from one to eight), the boards are stacked each on top of the other, and contained in the same compact shielded case in the final system assembly. The case will be connected to the receiving and transmitting antennas and to the power supply. The low-frequency output of the mixer, after low-pass filtering and amplification, is available for sampling, A/D conversion, and signal processing on the FPGA.

TABLE II

RADAR SENSOR FRONT-END: TRADEOFF AMONG RECEIVING CHANNELS M_R, POWER CONSUMPTION, COVERED RANGE D, TRANSMITTED POWER, RESOLUTIONS OF ANGLE $\Delta\theta$, CROSS RANGE R, AND DISTANCE d_R

M_R	R	$\Delta\theta$	P_{TX}=7 dBm		P_{TX} = 34.5 dBm	
			Power consumption	D, d_R	Power consumption	D, d_R
1	N/A	N/A	2.34 W	300 m, 30 cm	10.74 W	2 km, 2 m
4	3.83 m	9.4^0	5.97 W		14.37 W	
8	1.64 m	4.1^0	11.2 W		19.6W	

The scalability of the proposed system is increased by foreseeing an extra power stage board. For example, using the HMC952A power amplifier [61], it is possible to cover the X-band with a power gain of 33 dB. The transmitted output power at the antenna is up to 35 dBm (3.16 W) considering the saturated power P_{sat} and up to 34.5 dB (2.82 W) considering the output power 1-dB compression point, i.e., operating in a linear region with maximum 1-dB compression versus an ideal transfer curve. The third-order intercept output power is 43 dBm.

By adding this extra stage, as proved in Section VII, the maximum detection distance is 2 km. This extra covered range is paid in terms of an increased power consumption of 8.4 W (1.4-A current drained from a 6 V supply source). The power consumption of the sensor analog front-end, including the ADC, is reported in Table II as a function of the number of received channels M_R, considering both the configurations with 7- and 34.5-dBm transmitted output power. Table II also summarizes the maximum covered distance, D, the corresponding resolution d_R, the relevant angle resolution, and the cross-range resolution R at a radial distance of 23 m (the stopping distance for a speed of about 50 km/h).

It is to be noted that the bandwidth content of the beat signal at IF depends on the maximum covered range D according to (4). When adding the extra power amplifier stage, which allows reaching a longer distance D (from 300 m to 2 km), to keep the maximum f_{IF} value, the chirp rate of the waveform synthesizer has to be reduced from a value $K = 3.7 \cdot (10^{12}/s^2)$ to a value $K = 0.55 \cdot (10^{12}/s^2)$. In this way, we keep constant the Radar sensor sizing in terms of low-pass filter, T_{SW}, ADC sampling rate, but we achieve a coarse distance resolution of 2 m instead of 30 cm. Therefore, in the proposed sensing system, there is a constant ratio between the distance resolution and the maximum covered distance of 1/1000 (30-cm resolution at 300-m distance and 2-m resolution at 2-km distance)

$$f_{\mathrm{IF}} = -2 \cdot V_{\mathrm{MAX}}/\lambda + K \cdot 2 \cdot D/c. \tag{4}$$

Concerning the effect of the phase noise of the waveform synthesizer, as discussed in [62], in FMCW Radar, the phase noise can mask out targets. Indeed, targets are detected

at frequency offsets of the carrier. The phase noise also contributes to inaccuracy of the detected signals, which leads to uncertainty in the range measurement. However, in our case, the frequency generation in our transceiver has a very low phase noise of – 96 dBc/Hz at 1 kHz (−115 dBc/Hz at 10 kHz). In the mixer of an FMCW Radar receiver, the transmit signal is injected so that it can be mixed with the received signal. As discussed in [62], the phase noises of the transmitted and the received signals are to some degree correlated, and this effect can be exploited to improve the performance since at the output of the mixer is the difference that is important. As demonstrated in [62], the spectrum density of the phase noise difference [at the output of the mixer, which is the information digitized and processed by the fast Fourier transform (FFT)] is the spectrum density of the phase noise of the transmitted signal multiplied by a scaling factor SF in

$$\mathrm{SF} = 4 \cdot \sin^2(\pi \cdot l \cdot f_{\mathrm{OFF}}/c) \tag{5}$$

where the parameter l is the path length between the two signals, f_{OFF} is the frequency offset, and c is the speed of light. For example, at a frequency offset $f_{\mathrm{OFF}} = 1$ kHz and targeting a distance of 300 m, the reduction factor is 44 dB, i.e., the phase noise at the output of the mixer is −140 dBc/Hz. Such a noise contribution at the output of the mixer has not practical consequence in our system where the dynamic range is limited at 72 dB. Moreover, considering that for still targets, $f_{\mathrm{IF}} = K \cdot 2 \cdot D/c$ and being $K = 3.7 \cdot (10^{12}/s^2)$, in our case, the presence of spurious signals at an offset of 1 kHz in f_{IF} would correspond to a distance ambiguity of few centimeters, one order of magnitude lower than the 30-cm ambiguity due to the limited bandwidth. Summarizing, given the sizing of the present system, the phase noise in the waveforms generation is not a bottleneck.

V. Radar Sensor Signal Processing

The FMCW Radar sensor signal processing chain has been implemented using low-cost devices from the Xilinx Artix-7 FPGA family [63]. As discussed in Section IV, the Radar sensor mixed-signal front-end (receiver channels plus A/D multichannel converters) produces as output a digital signal containing information about the monitored area: if there is a target, its speed, range (i.e., distance along the radial direction), and cross-range position with a resolution depending on the number of channels. By converting the M_R received analog signals using an ADC working at 15 MS/s per channel with an ENOB of 12 b (a higher value of nominal bits is decimated at 12 b), a data rate of $M_R \cdot 180$ Mb/s is obtained. The data rate is 720 Mb/s and 1.44 Gb/s in the cases of four and eight receiving channels, respectively. This data flow may be processed by the FPGA-based section of the Radar sensor to detect possible obstacles inside the observation area and to extract speed, range, and cross-range measurements.

The first step is applying for each of the M_R receiving channels a 2-D FFT: first, a 1-D FFT is applied along each linear sweep of the FMCW received signal with a frequency resolution of about $1/T_{\mathrm{SW}} = 7.4$ kHz. Considering the input rate of 15 MS/s, this means a 1-D FFT of about 2030 samples. A power-of-two value of a 2048-point FFT is selected. The outputs of the first 1-D FFT are stored in a transpose RAM by row. The speed information due to Doppler shift can be obtained by observing the phase shift due to a target when multiple ramps in Fig. 2 are applied. As proved in [16], the number N_{ramp} of ramps depends on the maximum speed to be detected and on the speed resolution. Considering a maximum speed of 50 km/h and a speed resolution of 0.4 km/h, the number of sweeps and hence the number of rows is roughly 250. By selecting a power-of-two value of 256, a transpose memory of $256 \cdot 2048$ locations is required. With 256 ramps, if the maximum speed increases to 200 km/h, the speed resolution is 1.56 km/h. Along the 2048 columns, a 256-point FFT has to be applied, and as a result, a range-Doppler $256 \cdot 2048$ map is obtained. Peaks along the rows reveal the distance of a target, whereas peaks along the columns reveal the speed of the target. To this aim, a peak detection algorithm has to be used such as the cell averaging constant false alarm rate. The computational cost is mainly due to the 2048-point FFT that has to be calculated for all the 256 rows and the 256-point FFT that has to be calculated for the 2048 columns.

If cross-range information is also needed, together with range-Doppler map, then the above operations (2-D FFT plus peak detection) have to be repeated for each of the M_R channels. The phase difference of the radial distance and of the speed results of the M_R different channels can be used to estimate the target cross range, i.e., the position of the target in the azimuth direction. To this aim, a third 1-D FFT is required to be applied for all the $256 \cdot 2048$ M_R-point vectors of the range-Doppler-azimuth cube of data. As a global result, a 3-D FFT processing is needed. Considering, for example, $M_R = 4$, the memory required amounts to 2M words each of at least 24 b (12 ENOBs each for real and imaginary parts), i.e., about 50 Mb. By increasing the number of received channels to eight, the transpose memory increases to about 100 Mb. Fig. 3 summarizes the steps of this sensor signal processing chain and the data organization.

The computational cost of each N-point FFT to be calculated S times is $S \cdot N \cdot \mathrm{Log}_2 N$. Thus, (6) shows the number of multiply and accumulate (MAC) operations, considering M_R channels, to be calculated in a time slot of $N_{\mathrm{ramp}} \cdot T_{\mathrm{SW}} = 34.56$ ms for all the FFTs in the 3-D FFT. For the cases $M_R = 4$ and $M_R = 8$, the computational burden is $1.274 \cdot 10^9$ MAC and $2.67 \cdot 10^9$ MAC operations per second, respectively

$$\begin{aligned} &M_R \cdot [256 \cdot 2048 \cdot 11 + 2048 \cdot 256 \cdot 8] \\ &\quad + 2048 \cdot 256 \cdot M_R \cdot \mathrm{Log}_2 M_R. \end{aligned} \tag{6}$$

As an alternative, another approach is first solving for each ramp the range-azimuth detection problem with an $M_R \cdot 2048$ 2-D FFT processor. First, a 2048-point FFT has to be calculated for the M_R rows, and then an M_R-point FFT has to be repeated for the 2048 columns. This approach is useful to achieve a range-azimuth (cross-range) spatial image. Once successive frames are obtained, a motion detection algorithm operating in time [64] or in frequency domain can be used.

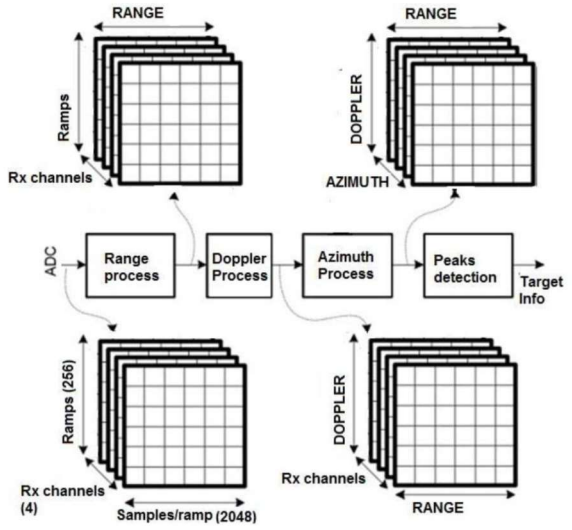

Fig. 3. Range-Doppler 2-D FFT sensor signal processing plus a third FFT along the channels for azimuth estimation and peak detection.

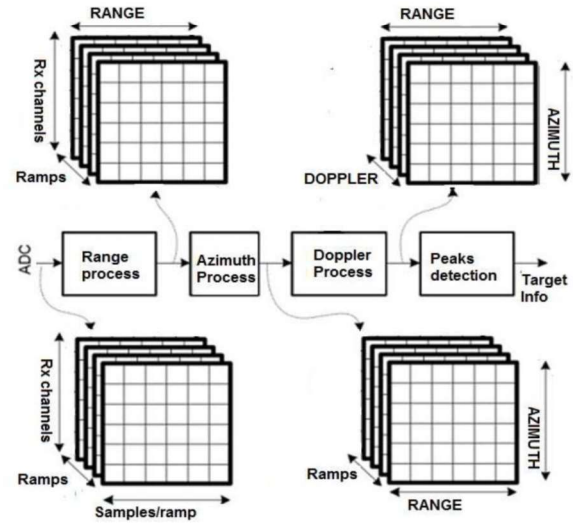

Fig. 4. Range-azimuth 2-D FFT sensor signal processing plus a third FFT for motion estimation in frequency domain and peak detection.

The motion estimation in the frequency domain can be implemented through an FFT [16]. By observing the target for 256 sweeps also in this case, a third FFT has to be applied for all the $M_R \cdot 2048$ 256-point vectors of the $M_R \cdot 2048 \cdot 256$ cube of data. All operations have to be conducted into the same time slot of $N_{\text{ramp}} \cdot T_{\text{SW}} = 34.56$ ms. Fig. 4 summarizes the steps of this sensor signal processing chain.

It can be demonstrated that the computational cost of this second data arrangement is the same as above. This second approach is useful when only a range-azimuth (cross range) spatial image is needed, from which thanks to a change of coordinates (from polar to cartesian ones) a conventional spatial image in the X-Y Cartesian space may be obtained.

The bottleneck for real-time Radar sensor signal processing, in this paper, is the pipeline processing of the three 1-D FFT blocks at 2048, 256, and 8 points, respectively. As far as the data size is concerned, the incoming complex samples to the FFT processor from the transceiver are digitized at 24 b (12 b for real and imaginary parts). The clock of the FPGA-based processor (see Section VI) implementing the 3-D FFT calculation is properly sized to implement in worst case all operations in a time slot of $N_{\text{ramp}} \cdot T_{\text{SW}} = 34.56$ ms, being $N_{\text{ramp}} = 256$ and $T_{\text{SW}} = 135$ μs.

A preliminary region of interest (ROI) selection task allows removing parts of the observed area that are not of interest, thus reducing the computational cost.

VI. FPGA-Based Sensor Signal Processing Chain

In this paper, differently from [7] and [8], adopting GPPs, or [11] and [65] using GPU high-parallel computing platforms, the sensor signal processing chain has been implemented with a single FPGA. The FPGA also implements the data gain calibration. The aim of this task is calibrating the Radar sensor to increase the robustness of the system to environmental variation, e.g., temperature variations, that may occur during its functioning. To implement the calibration unit, a special loopback path has been implemented inside the sensor. The transmitted signal is routed through this special path and sent back to be received, once digitalized, by the FPGA to perform the calibration operation as the antenna signal is received and to perform the diagnostics function. The same FPGA device also manages the low-level hardware interfaces of the system. Indeed, FPGAs allow for a better tradeoff in terms of computational power and power consumption than GPP and GPU. Moreover, the communication and computational cost requirements of Section V (less than 1.5-Gb/s transfer rate and less than $3 \cdot 10^9$ MAC operations per second) are within the capability of low-cost and low-power FPGA families such as the Artix-7.

The processing algorithm has been first prototyped in MATLAB environment, and then translated in HDL language. The FPGA devices belonging to the Artix-7 family are realized in 28-nm CMOS technology and are offered at a price comparable with Spartan6 low-cost family. With respect to Spartan6 FPGA family, the Artix-7 one has much higher resources in terms of digital signal processor blocks, each with a preadder, a 25×18 multiplier, final adder, and accumulator. Beside the DSP blocks, 740 in the XC7A200T device [63], this FPGA component has also combinatorial and sequential configurable logic (roughly 135 000 lookup tables and 270 000 flip–flops), 13.14 Mb of embedded block RAM, up to 16 transceivers capable of 3-Gb/s data transfer toward external hosts, and embedded SDRAM controller. Since 13.14 Mb of memory is lower than the 50 or 100 Mb required by a transpose memory with $M_R = 4$ or $M_R = 8$ receiving channels, then external SDRAMs have to be used.

There is also a control module that implements the interfaces of the FPGA with the multichannel ADC and starts the waveform generation. The control module also implements a unit to write and read from an on-board FLASH memory. This may allow storing the relevant processing intermediate

outputs in a nonvolatile memory, used to reload such data when needed (for example, when restoring from blackouts). Specific FPGA blocks implement the operations described in Section V. A pipeline cascade of the three 1-D FFT blocks is implemented. To avoid dependencies among range and Doppler and azimuth data, proper ping-pong buffers are used. They are mapped in external SDRAMs since each buffer has a size of 50 ($M_R = 4$) or 100 Mb ($M_R = 8$). Each of the 1-D FFT algorithms (2018-point FFT, 256-point FFT, and 4-point FFT or 8-point FFT depending on if $M_R = 4$ or $M_R = 8$ channels are used) was designed exploiting the digital macrocells we developed in [66].

The 256-point FFT is designed using a cascade of four radix-4 stages. The four-point FFT requires just one radix-4 stage. A mixed radix-2/radix-4 architecture is used for the 2018-point FFT (five radix-4 stages plus one final radix-2 stage) and for the eight-point FFT (one radix-4 stage plus one radix-2 stage). By running the FPGA clock at 250 MHz with an Artix-7 XC7A200T device, the required computations can be processed within the observation time of 34.56 ms. The power budget for the FPGA-based signal processing is about 1.15 W in case $M_R = 4$, where 0.15 W are due to static FPGA power consumption and for channel-independent functions such as diagnostic, calibration, management of interface versus the ADC, the transmitter, and an external host. The power budget for the FPGA-based signal processing is about 2.15 W in case $M_R = 8$. These FPGA power values have to be added to the power budget of Table II. Therefore, the whole power budget in the case of four receiving channels is from 7.12 to 15.52 W depending on the transmitted power and hence on the maximum covered distance. The above values increase to 13.35 and 21.75 W in the case of four channels. If the angular and hence the cross-range information is not of interest (the Radar sensor provides just target detection and a measure of its speed and radial distance), then the FPGA power consumption with $M_R = 1$ is about 0.4 W. In this case, the total power consumption budget is reduced to 2.74 W for 300-m maximum covered distance and 11.14 W for 2-km maximum covered distance.

VII. Applications of the Radar Sensor to Surveillance Transport Systems

Using the implemented scalable Radar sensor acquisition and processing platform, different FMCW Radar configurations can be implemented. All of them operate in the X-band for surveillance in mobility systems: the detected range is up to 300 m, with a resolution of 30 cm, when transmitting an output power up to 7 dBm (5 mW) and is up to 2 km, with a resolution of 2 m, when transmitting an output power up to 34.5 dBm (2.8 W). Single or multiple receiving channels can be used. Depending on the data flow used (that in Fig. 3 or 4), and stopping the FFT processing to the first two dimensions, the sensor can be used to obtain only a range-Doppler map, i.e., information on range and speed, or only a range-azimuth map, i.e., information on range and cross-range position.

For example, Fig. 5 shows the range and speed results of a test campaign held in the car parking of the Department of Information Engineering at Pisa University

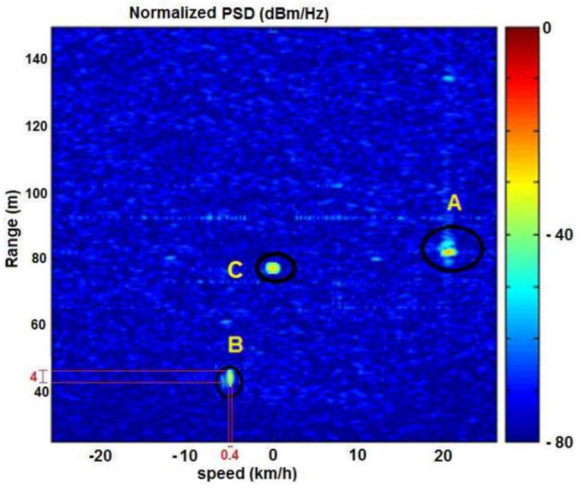

Fig. 5. Radar target detection in a car parking.

after the 2-D FFT has been applied and the range-Doppler map has been extracted. In the reported example, the Radar sensor was configured to process $M_R = 1$ receiving channel, with an output transmitted power of 0 dBm (1 mW) with a maximum distance of 150 m. Three different targets have been detected in this specific scene: Target A at a distance of 81 m and with a relative speed of 21 km/h, Target B at a distance of 44 m and a relative speed of 5.5 km/h, and Target C, almost still, at a distance of 77 m. The detected targets do not appear like a point in the range-doppler map, but rather like an oval. This is due to the physical size of the targets but also to the resolution limits in distance and speed of the Radar sensor (see Table I). As it is shown in Fig. 5 for Target B, thanks to a postprocessing step on the range-Doppler image, it is possible to extract the target size along the radial axis (4 m for Target B in Fig. 5, with a resolution limit of 30 cm) and the speed (5.5 km/h for Target B in Fig. 5, with an uncertainty of 0.4 km/h, due to the speed resolution limit). These experimental results demonstrate that the distance and speed resolution limits, derived from calculations in Sections III and IV and used for Radar design (see the report in Table I), can be obtained in real application scenarios. This is also due to the fact that the proposed Radar design is sized to reach maximum distances with an SNR at receiver side of about 20 dB. At the state of the art, there are works [67] demonstrating that 12 dB of SNR is enough for an FMCW Radar to detect vehicles. Therefore, the margin of several decibels in the SNR ensures that the expected performance from theoretical analysis can also be met in real-world applications.

To increase the safety of railroad or road urban crossing, the proposed Radar sensor has been configured to use all the receiving channels of the patch antenna. For the processing, first range-azimuth data have been extracted through the 2-D FFT. The proposed system also implements a data gain/offset calibration technique, discussed in [6]. Fig. 6 shows, when monitoring a railroad crossing, a sequence

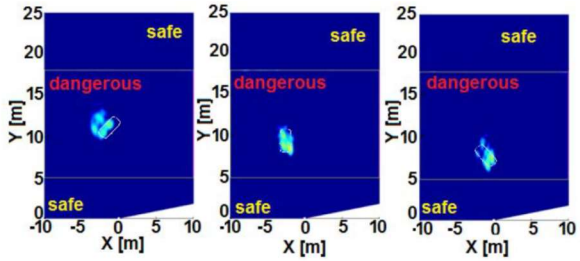

Fig. 6. Radar sensor output; car moving through a railroad crossing.

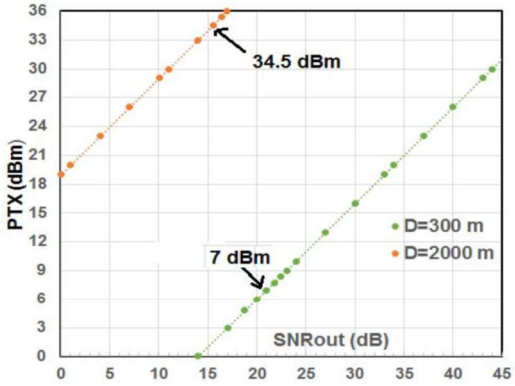

Fig. 7. Transmitted power needed to reach a given SNRout at the output of the digital processing chain at the receiver side.

of three images got after the ROI selection, range-zimuth map extraction, peak detection, and alarm decision. Before displaying the acquired image, a conversion from range-azimuth coordinates to Cartesian x-y coordinates is done. In Fig. 6, a car is detected when moving on a railway crossing in an area 20·25 m^2 at a distance of about 10 m. The dangerous zone (within the rails) and the safe zone (outside the rails) are also highlighted. The speed information is not needed in this case since the main objective is detecting the presence of an obstacle moving in the railway area. If speed information has to be extracted, this can be done in the frequency domain by applying the third 1-D FFT processor, as shown in Fig. 4.

Fig. 7 shows the transmitted power (dBm) that is needed to reach a given SNR at the output of the digital signal processing chain, considering two Radar configurations with maximum covered range of $D = 300$ m (30-cm resolution) and $D = 2000$ m (2-m resolution). In both cases, a target with a radar cross section of 1 m^2 has been considered, whereas for the maximum detected speed, we considered 130 km/h. Fig. 7 is obtained in the direction of maximum antenna gain, which is 13.4 dBi for the Fabry-Perot transmitting antenna and 12.2 dBi for the patch array receiving antenna. With 7 and 34.5 dBm in Fig. 7, the SNR value is at least 16 dB at the maximum distances.

Fig. 8 shows the result, in the case of a maritime application, of an acquisition, ROI selection, and range-speed map calculation for a ship entering a harbor at a speed below 5 knots (about 9 km/h). The detection distance in Fig. 8

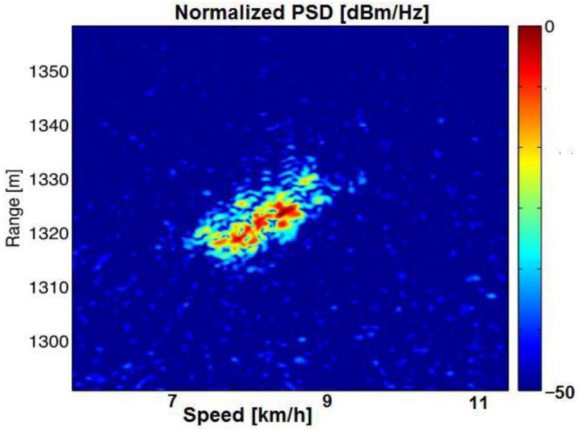

Fig. 8. ROI selection of a range-speed map for a maritime surveillance application.

is above 1.3 km. In maritime applications, the maximum speed can be limited to few tens of km/h since 20 knots is a typical ship cruise speed.

VIII. Conclusion

This paper has presented a scalable architecture for an acquisition and FPGA-based processing platform of a Radar sensor with a single transmitter and multiple receivers. The sensing system realizes an active sensor where an X-band transceiver emits frequency-modulated CWs with 7-dBm transmitted power. Adopting a 500-MHz bandwidth sweep around 10 GHz, a total observation period of 34.56 ms (256 ramps each for a time sweep of 135 μs) ensures a maximum sensing range of 300 m with a resolution of 30 cm. The angular resolution and the relevant cross-range resolution depend on the number of receiving channels. Using a scalable patch antenna array up to eight elements, an angular resolution of few degrees is obtained.

The received signals from the different acquisition channels are processed using a multidimensional FFT-based chain to extract range, azimuth, and Doppler information, i.e., position and speed of the target. An SNR of 20 dB is ensured at receiver output when transmitting 7 dBm (5 mW) at 300-m distance. By adding an extra power stage with 34.5-dBm (2.82 W) capability, the active sensing system can be configured to reach a target distance up to 2 km with a coarse resolution of 2 m, leaving all the rest of the hardware unchanged (the SNR at receiver side is about 15 dB).

The presented results show that the Radar sensor allows detecting moving and still targets in different mobility services like safe monitoring of railroad crossing, or in car parking, or in harbor monitoring. By changing the configurations in terms of number of receiving channels (which determines the angular and cross-range resolutions) and transmitted power (which determines the maximum sensing distance), the total power budget is from 2.74 W (one receiving channel and 7-dBm output power) to 21.75 W (eight receiving channels and 34.5-dBm output power). For the proposed Radar, the estimated cost and weight for a medium volume production (e.g., 10 000 pieces) is within 500 euros and 1 kg.

TABLE III
COMPARISON WITH STATE-OF-THE-ART RADAR AND LIDAR SENSORS

	Type	Power cons.	Range, resolution	Receiving Channels	Output power
This work	Radar X-band FMCW	2.74 W	300 m, 30 cm	1	7 dBm
This work	Radar X-band FMCW	11.14 W	2 km, 2 m	1	34.5 dBm
This work	Radar X-band FMCW	13.35 W	300 m, 30 cm	8	7 dBm
[42, 43]	Radar K-band Pulsed UWB	N/A	N/A	1	3 dBm
[17]	Radar Ku-band Pulsed	130 W	3.7 km, 5 m	N/A	40 dBm
[18]	Radar X-band Pulsed	N/A	45 km, N/A	N/A	75 dBm
[7]	Radar X-Band FMCW	>100 W	1200 m, 40 cm	3	33 dBm
[69]	Radar S-Band FMCW	N/A	100m, 20 cm	4	20 dBm
[19]	Radar V-band FMCW	N/A	<3.5 m, N/A	N/A	N/A
[70]	Radar X-band FMCW	650 W	50 km, 15 m	1	50 dBm
[51]	Radar C-Band FMCW	3 W	3 m, N/A	1	11 dBm
[31]	Lidar	12W	100 m,2 cm	N/A	N/A
[71]	Lidar	20 W	80 m, 2 cm	N/A	N/A
[44]	Radar W-band FMCW	4 W	200m, 10 cm	4	7 dBm
[10]	Radar W-band FMCW	20 W	200m, 25 cm	N/A	12 dBm
[68]	Radar Ku-band Pulsed	N/A	20 m, 5 cm	1	30 dBm

Table III compares this paper with the state of the art of Lidars and Radars operating in the range from few gigahertz to 77 GHz.

With respect to the Velodyne Lidars, also adopted in the Google autonomous car [1], the proposed Radar achieves a worst distance accuracy (tens of centimeters in the best case instead of few centimeters for Lidars) but a much higher detection range, up to 2 km, instead of 100 m only for Lidars. The power consumption of the proposed Radar in its worst case is comparable with that of state-of-the-art Lidars.

Low-power Radar sensing platforms have been proposed in the literature, but with a detection range of few meters. For example, let us consider the proposals of reusing for Radar the 60-GHz front-end and the powerful DSP processor already available in the next generation of smart phones in [19]–[21] or the Radar sensor for contactless vital signs measurements in [22]–[25] and [49]–[55]. With respect to these works, the design proposed in this paper has performances (detection range up to 300 m with a resolution of 30 cm, emitting only 7 dBm at the output) suited for smart mobility applications.

Analyzing the literature of long-range surveillance Radar sensors, most of them [17], [18], [70] are sized for much higher peak power. For example, the pulse compression Radar in [17] operating in Ku-band with a transmitted power of 8 W has a detection range from 20 m to 3.7 km with targets with RCS of few square meters. The range resolution is 5 m. The total power consumption is 130 W and the weight is 35 kg. The Radar in [18] allows for a 45-km covered range but emitting peak power pulses up to 32 kW. A maximum distance of 50 km is also reached in [70] reducing the emitted power at 100 W thanks to the use of the FMCW technique in X-band. However, the overall power consumption of 650 W and the resolution, limited to 15 m, make the Radar in [70] unsuited for the target applications of this paper. With respect to other Radars in X-band [7], the proposed design ensures a much lower power consumption. In [7], the power consumption is higher than 100 W targeting a 1.5-km distance, whereas in our case, the power consumption is from 2.74 to 21.75 W depending on the configuration. When comparing this paper with the X-band Radar discussed in [16, Ch. 6], it is worth noting that this paper refers to a complete Radar solution (TX and RX antennas plus transceiver, ADC, and FPGA real-time signal processing). Instead, [16] describes only the transceiver and misses the design of the antenna, of the ADC, and of the FPGA-based digital signal processing and control. Moreover, the transceiver in [16] is sized for a bandwidth of 300 MHz leading to a resolution of 50 cm, whereas in this paper, the waveform synthesizer is sized to provide an increased FMCW bandwidth of 500 MHz, which allows for a better resolution of 30 cm. Furthermore, the power amplifier in [16] refers to a fixed transmitted power of 10 W, whereas this paper implements a configurable solution allowing for different tradeoffs between Radar performance (maximum target distance and output SNR) and overall power consumption.

With respect to 77–79-GHz Radars, as in [10] and [44], the proposed work stands for a much larger covered distance, roughly one order of magnitude (from 200 to 250 m in [10] and [44] to 2 km in this design) for comparable power budget. This is a key characteristic to adopt the Radar as a ubiquitous sensor to be installed not also in fixed positions, but also on-board vehicles such as cars or UAVs. Future work in this direction will be related to the characterization of the proposed Radar sensing system in the harsh operating conditions of aerial and land vehicles [72].

ACKNOWLEDGMENT

The authors would like to thank R. Massini. M. Martorella, F. Berizzi, S. Lischi, and D. Staglianò from CNIT-RASS for discussions as well as R. Piernicola and M. Righetto from IDS spa for discussions in the field of the EU-FESR project SIMPLE.

REFERENCES

[1] A. Mukhtar, L. Xia, and T. B. Tang, "Vehicle detection techniques for collision avoidance systems: A review," *IEEE Trans. Intell. Transp. Syst.*, vol. 16, no. 5, pp. 2318–2338, Oct. 2015.

[2] L. D. Baskar, B. D. Schutter, J. Hellendoorn, and Z. Papp, "Traffic control and intelligent vehicle highway systems: A survey," *IET Intell. Transp. Syst.*, vol. 5, no. 1, pp. 38–52, Mar. 2011.

[3] H. Zhou, H. Kong, L. Wei, D. Creighton, and S. Nahavandi, "Efficient road detection and tracking for unmanned aerial vehicle," *IEEE Trans. Intell. Transp. Syst*, vol. 16, no. 1, pp. 297–309, Feb. 2015.

[4] T. Horimatsu, "ITS sensor for railroad crossing safety," *Fujitsu Sci. Tech. J.*, vol. 43, no. 2, pp. 220–226, 2007.

[5] R. Ramchadran, "FPGA based SoC for railway level crossing management system," *Int. J. Soft Comput. Eng.*, vol. 2, no. 3, pp. 134–137, 2012.

[6] S. Saponara, L. Fanucci, R. Cassettari, R. Piernicola, and M. Righetto, "Networked radar system to increase safety of urban railroad crossing," in *Proc. WASET ICSUTE*, Paris, France, 2015, pp. 450–455.

[7] S. Lischi *et al.*, "X-band compact low cost multi-channel radar prototype for short range high resolution 3D-InISAR," in *Proc. IEEE EuRAD*, Oct. 2014, pp. 157–160.

[8] D. Staglianò, E. Giusti, S. Lischi, and M. Martorella, "3D InISAR-based target reconstruction algorithm by using a multi-channel ground-based radar demonstrator," in *Proc. IEEE Int. Radar Conf.*, Oct. 2014, pp. 1–6.

[9] D. Göhring, M. Wang, M. Schnürmacher, and T. Ganjineh, "Radar/lidar sensor fusion for car-following on highways," in *Proc. IEEE ICARA*, Dec. 2011, pp. 407–412.

[10] J. Johnston, "Off-highway obstacle detection," *IEEE Instrum. Meas. Mag.*, vol. 9, no. 5, pp. 16–24, Oct. 2006.

[11] A. Mammeri, T. Zuo, and A. Boukerche, "Extending the detection range of vision-based vehicular instrumentation," *IEEE Trans. Instrum. Meas.*, vol. 65, no. 4, pp. 856–873, Apr. 2016.

[12] R. G. Lins, S. N. Givigi, and P. R. G. Kurka, "Velocity estimation for autonomous vehicles based on image analysis," *IEEE Trans. Instrum. Meas.*, vol. 65, no. 1, pp. 96–103, Jan. 2016.

[13] M. Skolnik, *Introduction to Radar Systems*, 3rd ed. New York, NY, USA: McGraw-Hill, 2001.

[14] B. Neri and S. Saponara, "Advances in technologies, architectures, and applications of highly-integrated low-power radars," *IEEE Aerosp. Electron. Syst. Mag.*, vol. 27, no. 1, pp. 25–36, Jan. 2012.

[15] L. Hawkins *et al.*, "Radar defense vs. automotive," in *Proc. EuMW Defense Forum*, 2013, pp. 1–37.

[16] S. Saponara, E. Ragonese, M. Greco, B. Neri, and G. Palmisano, *Highly Integrated Low-Power Radars*. Norwood, MA, USA: Artech House, 2014, p. 232.

[17] *Data Sheet, Scanter 1002 Ground Surveillance Radar*, Terma A/S, Chesapeake, VA, USA, 2015

[18] *Data Sheet, SLAR9000: Side Looking Airborne Radar*, Terma A/S, Chesapeake, VA, USA, 2015.

[19] Y. Zhu, Y. Zhu, B. Y. Zhao, and H. Zheng, "Reusing 60GHz radios for mobile radar imaging," in *Proc. ACM MobiCom*, Paris, France, 2015, pp. 103–116.

[20] Y. Zhu, Y. Zhu, Z. Zhang, B. Y. Zhao, and H. Zheng, "60GHz mobile imaging radar," in *Proc. ACM HotMobile*, Santa Fe, NM, USA, Feb. 2015, pp. 65–80.

[21] T.-Y. J. Kao and J. Lin, "Vital sign detection using 60-GHz Doppler radar system," in *Proc. IEEE Int. Wireless Symp.*, Apr. 2013, pp. 1–4.

[22] D. Zito *et al.*, "SoC CMOS UWB pulse radar sensor for contactless respiratory rate monitoring," *IEEE Trans. Biomed. Circuits Syst.*, vol. 5, no. 6, pp. 503–510, Dec. 2011.

[23] C. Li, X. Yu, C.-M. Lee, D. Li, L. Ran, and J. Lin, "High-sensitivity software-configurable 5.8-GHz radar sensor receiver chip in 0.13-μm CMOS for noncontact vital sign detection," *IEEE Trans. Microw. Theory Techn.*, vol. 58, no. 5, pp. 1410–1419, May 2010.

[24] E. Piuzzi, S. Pisa, P. D'Atanasio, and A. Zambotti, "Radar cross section measurements of the human body for UWB radar applications," in *Proc. IEEE Int. Instrum. Meas. Technol. Conf. (I2MTC)*, May 2012, pp. 1290–1293.

[25] E. Piuzzi, P. D'Atanasio, S. Pisa, E. Pittella, and A. Zambotti, "Complex radar cross section measurements of the human body for breath-activity monitoring applications," *IEEE Trans. Instrum. Meas.*, vol. 64, no. 8, pp. 2247–2258, Aug. 2015.

[26] T. Huang, P. V. Brennan, D. Patrick, I. Weller, P. Roberts, and K. Hughes,, "FMCW based MIMO imaging radar for maritime navigation," *Prog. Electromagn. Res.*, vol. 115, pp. 327–342, Apr. 2011.

[27] S. Saponara and B. Neri, "Radar sensor signal acquisition and 3D FFT processing for smart mobility surveillance systems," in *Proc. IEEE Sens. Appl. Symp.*, Apr. 2016, pp. 1–6.

[28] J. Pallauf, J. Wagner, and F. P. León, "Evaluation of state-dependent pedestrian tracking based on finite sets," *IEEE Trans. Instrum. Meas.*, vol. 64, no. 5, pp. 1276–1284, May 2015.

[29] Y. Li, Y. Ruichek, and C. Cappelle, "Optimal extrinsic calibration between a stereoscopic system and a LIDAR," *IEEE Trans. Instrum. Meas.*, vol. 62, no. 8, pp. 2258–2269, Aug. 2013.

[30] Z. Hu, Y. Li, N. Li, and B. Zhao, "Extrinsic calibration of 2-D laser rangefinder and camera from single shot based on minimal solution," *IEEE Trans. Instrum. Meas.*, vol. 65, no. 4, pp. 915–929, Apr. 2016.

[31] *High-Definition Real-Time 3D LIDAR*, document 97-0038 rev. F, Velodyne Lidar HDL32, 2016, pp. 1–2.

[32] R. Lamb, "Long-range 3D imaging lidar," *SPIE Newsroom*, pp. 1–2, Apr. 10, 2014, doi: 10.1117/2.1201404.005422.

[33] R. A. Lamb, P. A. Hiskett, and R. A. Lamb, "Advanced 3D imaging lidar concepts for long range sensing," *Proc. SPIE*, vol. 9114, p. 91140G, Jun. 2014.

[34] *Kestrel 32x32 Geiger-Mode Flash 3-D LIDAR Camera*, accessed on Sep. 7, 2016. [Online]. Available: http://www.princetonlightwave.com/wp-content/uploads/2016/09/PLI-Kestrel.pdf

[35] *SpectroScan 3D MEMS LIDAR System Model MLS 201*, accessed on Sep. 7, 2016. [Online]. Available: http://www.spectrolab.com/sensors/pdfs/products/SPECTROSCAN3D_RevA%20071912.pdf

[36] R. M. Marino and W. R. Davis, Jr., "Jigsaw: A foliage-penetrating 3D imaging laser radar system," *Lincoln Lab. J.*, vol. 15, no. 1, pp. 23–36, 2005.

[37] S. Shirmohammadi and A. Ferrero, "Camera as the instrument: The rising trend of vision based measurement," *IEEE Instrum. Meas. Mag.*, vol. 17, no. 3, pp. 41–47, Jun. 2014.

[38] J. J. Garcia, Á. Hernández, J. Ureña, and E. García, "FPGA-based architecture for a multisensory barrier to enhance railway safety," *IEEE Trans. Instrum. Meas.*, vol. 65, no. 6, pp. 1352–1363, Jun. 2016.

[39] *The World's First Intelligent Thermal Sensor for Rail Transport Safety*, document IT_0021_EN, FLIR Thermirail, 2016, pp. 1–2.

[40] S. Scherr, S. Ayhan, B. Fischbach, A. Bhutani, M. Pauli, and T. Zwick, "An efficient frequency and phase estimation algorithm with CRB performance for FMCW radar applications," *IEEE Trans. Instrum. Meas.*, vol. 64, no. 7, pp. 1868–1875, Jul. 2015.

[41] O. Postolache, J. M. D. Pereira, V. Viegas, and P. S. Girão, "Gait rehabilitation assessment based on microwave Doppler radars embedded in walkers," in *Proc. IEEE MeMeA*, May 2015, pp. 208–213.

[42] V. Giammello, E. Ragonese, and G. Palmisano, "A 24/77-GHz SiGe BiCMOS transmitter chipset for automotive radar," *Microw. Opt. Technol. Lett.*, vol. 55, no. 4, pp. 782–786, 2013.

[43] E. Ragonese, A. Scuderi, V. Giammello, and G. Palmisano, "A SiGe BiCMOS 24-GHz receiver front-end for automotive short-range radar," *Analog Integr. Circuits Signal Process.*, vol. 67, no. 2, pp. 121–130, 2011.

[44] J. Hatch, A. Topak, R. Schnabel, T. Zwick, R. Weigel, and C. Waldschmidt, "Millimeter-wave technology for automotive radar sensors in the 77 GHz frequency band," *IEEE Trans. Microw. Theory Techn.*, vol. 60, no. 3, pp. 845–860, Mar. 2012.

[45] E. Hyuun, W. Oh, and J.-H. Lee, "Design and implementation of automotive 77GHz FMCW radar system based on DSP and FPGA," in *Proc. IEEE ICCE*, Jan. 2011, pp. 517–528.

[46] C. Baer, T. Jaeschke, N. Pohl, and T. Musch, "Contactless detection of state parameter fluctuations of gaseous media based on an mm-Wave FMCW radar," *IEEE Trans. Instrum. Meas.*, vol. 64, no. 4, pp. 865–872, Apr. 2015.

[47] V. Gregers-Hansen, *Radio Propagation at 90 GHz, FCC Forum New Horizons: 90 GHz Technologies*, document FCC 16-89, 2000, pp. 1–21.

[48] G. Rubio-Cidre, A. Badolato, L. Úbeda-Medina, J. Grajal, B. Mencia-Oliva, and B.-P. Dorta-Naranjo, "DDS-based signal-generation architecture comparison for an imaging radar at 300 GHz," *IEEE Trans. Instrum. Meas.*, vol. 64, no. 11, pp. 3085–3098, Nov. 2015.

[49] J. Kranjec, S. Beguš, J. Drnovšek, and G. Geršak, "Novel methods for noncontact heart rate measurement: A feasibility study," *IEEE Trans. Instrum. Meas.*, vol. 63, no. 4, pp. 838–847, Apr. 2014.

[50] S. Kazemi, A. Ghorbani, H. Amindavar, and D. R. Morgan, "Vital-sign extraction using bootstrap-based generalized warblet transform in heart and respiration monitoring radar system," *IEEE Trans. Instrum. Meas.*, vol. 65, no. 2, pp. 255–263, Feb. 2016.

[51] J. Tu and J. Lin, "Fast acquisition of heart rate in noncontact vital sign radar measurement using time-window-variation technique," *IEEE Trans. Instrum. Meas.*, vol. 65, no. 1, pp. 112–122, Jan. 2016.

[52] J. Wang, X. Wang, L. Chen, J. Huangfu, C. Li, and L. Ran, "Noncontact distance and amplitude-independent vibration measurement based on an extended DACM algorithm," *IEEE Trans. Instrum. Meas.*, vol. 63, no. 1, pp. 145–153, Jan. 2014.

[53] S. S. Stuchly, M. S. Sabir, and A. Hamid, "Advances in monitoring of velocities and densities of particulates using microwave Doppler effect," *IEEE Trans. Instrum. Meas.*, vol. 26, no. 1, pp. 21–24, Mar. 1977.

[54] Á. Parra-Cerrada, V, González-Posadas, J. Luis Jiménez-Martín, Á. Blanco-del-Campo, W. Hernandez, and C. Calderón-Córdova, "Low-cost measurement for a secondary mode S radar transmitter," *IEEE Trans. Instrum. Meas.*, vol. 64, no. 12, pp. 3217–3225, Dec. 2015.

[55] Y. Yang, C. Gu, Y. Li, R. Gale, and C. Li, "Doppler radar motion sensor with CMOS digital DC-tuning VGA and inverter-based sigma-delta modulator," *IEEE Trans. Instrum. Meas.*, vol. 63, no. 11, pp. 2666–2674, Nov. 2014.

[56] F. Tampieri and C. Tomasi, "Size distribution models of fog and cloud droplets and their volume extinction coefficients at visible and infrared wavelengths," *Pure Appl. Geophys.*, vol. 114, no. 4, pp. 571–586, 1976.
[57] S. N. Bhuiya, F. Islam, and M. A. Matin, "Analysis of direction of arrival techniques using uniform linear array," *Int. J. Comput. Theory Eng.*, vol. 4, no. 6, pp. 931–934, 2012.
[58] N. Wang, Q. Liu, C. Wu, L. Talbi, Q. Zeng, and J. Xu, "Wideband fabry-perot resonator antenna with two complementary FSS layers," *IEEE Trans. Antennas Propag.*, vol. 62, no. 5, pp. 2463–2471, May 2014.
[59] *LMX2492/LMX2492-Q1: 14 GHz Low Noise Fractional N PLL With Ramp/Chirp Generation*, document SNAS624B, Texas Instruments, 2015.
[60] *RFVC1842: 9.3 GHz to 10.7 GHz MMIC VCO With Fo/2 and Fo/4 Outputs*, document Data Sheet DS140428, RFMD Inc, 2013, pp. 1–10.
[61] *HMC952ALP5GE Data Sheet, V0.1*, Analog Devices, Norwood, MA, USA, Dec. 2015.
[62] R. Undheim, "Design of a linear FMCW radar synthesizer with focus on phase noise," M.S. thesis, Dept. Electron. Telecommun., Norwegian Univ. Sci. Technol., Trondheim, Norway, 2012.
[63] *7 Series FPGA Overview*, document DS180, v1.17, Xilinx, 2015, pp. 1–17.
[64] S. Saponara, M. Martina, M. Casula, L. Fanucci, and G. Masera, "Motion estimation and CABAC VLSI co-processors for real-time high-quality H.264/AVC video coding," *Microprocess. Microsyst.*, vol. 34, nos. 7–8, pp. 316–328, 2010.
[65] L. Tirado, G. Ghazi, J. Á. Martínez-Lorenzo, C. M. Rappaport, Y. Álvarez, and F. Las-Heras, "A GPU implementation of the inverse fast multipole method for multi-bistatic imaging applications," in *Proc. IEEE APURSI*, Jul. 2014, pp. 874–875.
[66] N. E. L'Insalata, S. Saponara, L. Fanucci, and T. Pierangelo, "Automatic synthesis of cost effective FFT/FFT cores for VLSI OFDM systems," *IEICE Trans. Electron.*, vol. E91-C, no. 4, pp. 487–496, 2008.
[67] V. Issakov, *Microwave Circuits for 24GHz Automotive Radar in Silicon-Based Technologies*. Berlin, Germany: Springer-Verlag, 2010.
[68] J.-H. Choi, J.-H. Jang, and J.-E. Roh, "Design of an FMCW radar altimeter for wide-range and low measurement error," *IEEE Trans. Instrum. Meas.*, vol. 64, no. 12, pp. 3517–3525, Dec. 2015.
[69] W. Wang, D. Liang, Z. Wang, H. Yu, and Q. Liu, "Design and implementation of a FPGA and DSP based MIMO radar imaging system," *Radioengineering*, vol. 24, no. 2, pp. 518–526, 2015.
[70] B. Isom, J. Helvin, M. Jones, and M. Knight, "A new compact polarimetric solid-state X-band radar: System description and performance analysis," in *Proc. 93rd AMS Annu. Meeting*, Jan. 2013, pp. 5–10.
[71] *Laser Measurement Systems LMS200 to LMS291*, document 8008970/QI72/2006-12, Sick Inc., 2006, pp. 1–48.
[72] S. Saponara, E. Petri, L. Fanucci, and P. Terreni, "Sensor modeling, low-complexity fusion algorithms, and mixed-signal IC prototyping for gas measures in low-emission vehicles," *IEEE Trans. Instrum. Meas.*, vol. 60, no. 2, pp. 372–384, Feb. 2011.

Sergio Saponara (SM'12) received the master's and Ph.D. (*cum laude*) degrees in electronic engineering from the University of Pisa, Pisa, Italy, in 1999 and 2003, respectively.

He was a Marie Curie Research Fellow at the Interuniversity Microelectronics Center, Leuven, Belgium. He is currently a Professor of Electronics with the University of Pisa and with the Italian Naval Academy, Livorno, Italy. He is also the Chief Technical Officer and Co-Founder at IngeniArs srl, Pisa. He is the Scientific Manager of the Enabling Technologies for the Internet of Things at Pisa University. He has co-authored more than 250 scientific publications on international journals and conferences, and holds about 20 patents.

Dr. Saponara is a member of the IEEE Instrumentation and Measurement Society. He was involved in organizing committees of about 100 IEEE and SPIE conferences. He is an Associate Editor of the Springer's *Journal of Real-Time Image Processing*, *IET Electronics Letters*, *MDPI Designs*, and *Journal of Wireless Communications*.

Bruno Neri is currently a Professor of Radio-frequency Electronics, Instrumentation, and Measurements with the University of Pisa, Pisa, Italy, where he is also the Director of the RF and Microwave IC Laboratory, the President of the bachelor and master degree courses in electronic engineering, and the Director with the Department of Information Engineering. He has co-authored about 150 scientific publications on international journals, conferences, and patents.

Dr. Neri is a member of the governing body of the Italian National Association for Electronics GE.